Energy & Environmental Science

Cite this: *Energy Environ. Sci.*, 2012, **5**, 7913

www.rsc.org/ees

COMMUNICATION

Raman spectroscopic monitoring of carbon deposition on hydrocarbon-fed solid oxide fuel cell anodes†

Kevin S. Blinn,[a] Harry Abernathy,‡[a] Xiaxi Li,[a] Mingfei Liu,[a] Lawrence A. Bottomley[b] and Meilin Liu*[a]

Received 28th February 2012, Accepted 9th May 2012
DOI: 10.1039/c2ee21499g

Solid oxide fuel cells (SOFCs) are potentially the most efficient and cost-effective solution for the utilization of a wide variety of fuels beyond hydrogen. One of the chief obstacles to true fuel flexibility lies in anode deactivation by coking as well as a limited mechanistic understanding of coking and its prevention. Here we report Raman spectroscopic *mapping* and *monitoring* of carbon deposition on SOFC anode surfaces under both *ex situ* and *in situ* conditions. Carbon mapping was successfully demonstrated with a model Ni–YSZ electrode exposed to a CH_4-containing atmosphere at high temperature (625 °C), while carbon deposition over time in a wet C_3H_8 atmosphere was directly monitored on a similar anode system as well as a BaO-modified system. This spectroscopic technique provides valuable insight into the mechanism of carbon deposition, which is vital in achieving rational design of carbon-tolerant anode materials.

[a]*School of Materials Science and Engineering, Center for Innovative Fuel Cell and Battery Technologies, Georgia Institute of Technology, Atlanta, GA 30332-0245, USA. E-mail: meilin.liu@mse.gatech.edu*
[b]*School of Chemistry and Biochemistry, Georgia Institute of Technology, Atlanta, GA 30332-0400, USA*

† Electronic supplementary information (ESI) available. See DOI: 10.1039/c2ee21499g

‡ Current address: National Energy Technology Laboratory, Morgantown, WV 26507-0880, USA.

Solid oxide fuel cells (SOFCs) represent one of the cleanest, most efficient, and most versatile electrical energy production systems.[1] Unlike most other types of fuel cells, SOFCs may employ catalyst materials that give them the ability to utilize both hydrogen (H_2) and hydrocarbon fuels by virtue of their high operating temperatures (400–1000 °C). Thus, when using familiar fossil fuels as well as renewable fuels, SOFCs can give access to greater energy harvests as well as highly reduced emissions (*e.g.*, CO_2, SO_x, NO_x, and other harmful species) as compared to conventional combustion.[2–4]

Unfortunately, supplying SOFCs with hydrocarbon fuels poses many problems for systems using state-of-the-art material specifications, such as ceramic–metal composites (cermets) of Ni and yttria-stabilized zirconia (YSZ). Ni, the most common active component of anode materials used for SOFCs and for reforming of hydrocarbon fuels, is very prone to carbon deposition on its surface, or "coking."[5,6] Even supplying a conventional Ni-anode SOFC with the low-order hydrocarbons (*i.e.* CH_4 and C_3H_8) contained in natural gas tends to result in very aggressive coking with blocking of active reaction sites and quick anode performance degradation.[3]

To make SOFCs truly fuel-flexible and candidates for more effective power systems, the issue of anode coking tolerance needs to be addressed. Anode materials and structures beyond traditional cermets have been explored by SOFC researchers to this end.[3,4,7–12] Recently, a new material, $BaZr_{0.1}Ce_{0.7}Y_{0.1}Yb_{0.1}O_{3-\delta}$ (BZCYYb), was reported to provide the anode with excellent tolerance to coking under SOFC operating conditions in the presence of moisture.[3] Other

Broader context

The rates of many chemical and energy transformation processes that take place in energy storage and conversion devices (*e.g.* fuel cells) are limited primarily by charge and mass transfer along surfaces and across interfaces. Unfortunately, the mechanistic understanding of these processes is still lacking, due largely to the difficulty of characterizing these processes under *in situ* conditions. The development of new tools for probing and mapping surface chemistries relevant to electrode reactions is vital to unravel the mechanisms of surface processes and to achieve rational design of new materials for efficient energy storage and conversion. Among the relatively few *in situ* surface analysis methods, Raman spectroscopy can be performed even in the presence of harsh atmospheres at high temperatures. It can also be used alongside electrochemical measurements, potentially allowing direct correlation of electrochemistry to surface chemistry in an operating cell. Raman spectroscopy has been successfully used to map carbon *ex situ*, and Raman's ability to detect relevant species and phases under *in situ* conditions has been demonstrated thus far. Still, proper *in situ* mapping measurements would be most useful for pin-pointing important reaction mechanisms. The current work demonstrates significant progress towards this capability. The technique presented herein is applicable to *in situ* characterization of other energy storage and conversion systems that also involve carbon (*e.g.* batteries and pseudocapacitors).

alternatives with appreciable coking tolerance, such as (La,Sr)$TiO_{3-\delta}$,[7,8] $Sr_2(Mn,Mg)MoO_{6-\delta}$,[9] liquid Sn,[10] and Cu-based[11,12] anodes, have been proposed as well. Unfortunately, the chief problems facing their applicability to fuel cell systems lie in physical, chemical, and thermal incompatibilities with state-of-the-art YSZ electrolyte, relatively high cost, and lower overall catalytic performance. On the other hand, efforts have been made to improve the coking tolerance of more conventional Ni–YSZ by modifying the surface of Ni with nanostructured "islands" of BaO[4] and Y-doped $BaZrO_3$ coatings.[13]

Some questions remain on how such modification conveys coking resistance to the anode. In the case of the BaO nanoparticles, one hypothesis revolves around the considerable affinity of BaO for water. According to DFT calculations performed for this material,[4] nanoscale particles of BaO are capable of water adsorption. The adsorbed water can subsequently dissociate and form hydroxyl groups which may migrate to the Ni surface and assist in removing carbon from the Ni surface that is deposited by the cracking or pyrolysis of the hydrocarbon fuel. An improved understanding of this tolerance mechanism, such as knowledge of how and where the carbon deposits on the Ni electrode surface and how far away from the nanostructures the carbon removal effect happens, is vital to a more optimized design of coking-tolerant anodes. Obtaining such information requires direct observation and quantification of the carbon as it deposits on the anode surface under relevant operating conditions.

Raman spectroscopy is a surface analysis technique ideally suited for gathering this information. It possesses large flexibility in terms of conditions under which it can be performed, including the harsh temperatures and atmospheres inherent to SOFC anode operation.[14] In addition, it is quite sensitive to a vast variety of chemical species, including different forms of carbon,[15–24] hydrocarbons,[25] oxygen,[26–28] and water.[3,4] Moreover, Raman spectroscopy can potentially be used alongside electrochemical measurements to probe surface species and phases of interest (*e.g.* anode reaction intermediates and products), allowing the direct correlation of electrochemical performance to anode surface chemistry.

Raman spectroscopy has been shown to be an effective tool for studying a variety of SOFC materials through a collection of recent research efforts, including investigations of oxidation states in Gd-doped ceria (GDC) electrolytes under reducing atmosphere,[29] modification of glass sealants for SOFC systems,[30] Cr poisoning of cathodes for cells that have metallic interconnects,[31] and H_2S poisoning of Ni-based anodes.[32–34] In particular, studies of coking on SOFC anodes operating under carbon-containing fuels have demonstrated the sensitivity of Raman spectroscopy to carbon species and its ability to distinguish between different forms of carbon bonding.[15–20,23] Walker *et al.* first developed and demonstrated a Raman microscopy system that was capable of *in situ* detection of coking on Ni–YSZ anodes.[18–20] Since then, others have adapted this methodology for similar investigations.[21] In addition, surface-enhanced Raman methods have been used to further increase the sensitivity of Raman spectroscopy to carbon on anode surfaces.[24]

To truly understand coking-related degradation and tolerance mechanisms for SOFC anodes, the ability to effectively *map* the location and form of the deposited carbon with adequate spatial resolution is needed. Yoshinaga *et al.* demonstrated *ex situ* Raman mapping of carbon on Ni.[22] In addition, Pomfret, Owrutsky, and co-workers have developed near-infrared thermal imaging techniques for monitoring coking-related degradation in SOFCs operated on alkane and alcohol fuels.[20,35] In the current work, we report our most recent efforts to expand upon this information even further by improved mapping and monitoring of carbon deposited both *ex situ* and *in situ* on Ni-based anodes with and without coking-tolerant surface modifications. For comparison purposes, Cu anodes were also evaluated. Cu anodes have been shown to be much less active towards coking than Ni.[12]

Ni coupons were used to study how coking varies over a polycrystalline Ni surface. For a larger portion of this investigation, electrodes having well-defined boundaries with YSZ electrolyte material were employed to resolve phase boundaries. Further details on sample preparation and analysis can be found in the ESI†.

Microscale patterned Ni and Cu strips that were deposited on YSZ substrates using photolithography methods[36,37] as well as a Ni mesh embedded in YSZ served these purposes. *In situ* experiments were performed using an environmental chamber designed for direct Raman analysis of samples under high temperature and fuel gas atmosphere (Fig. ESI-1†). This study puts some emphasis on studying coking on Ni-based SOFC anodes from low-order alkane fuels, namely CH_4 and C_3H_8.

Fig. 1 displays a portion of a typical Raman spectrum collected *ex situ* from a heavily coked spot on a Ni coupon following exposure to C_3H_8-containing gas at 550 °C. Over the 1200–1750 cm^{-1} region, the spectrum contains three primary features at 1357 cm^{-1} ("D-band"), 1585 cm^{-1} ("G-band"), and 1617 cm^{-1} ("D′-band"). The G-band corresponds to C–C stretching that is common to all sp^2-bonded carbons, while the D-band and D′-band features reflect disorder in the structure of the deposited carbon.[16] Raman features related to the D-band were the focus of the *ex situ* mapping studies; although the G-band was at times the spectral feature of greater intensity, some samples contained YSZ, whose characteristic Raman spectrum contains a broad peak in the same wavenumber range as the G-band when collected at room temperature. A corresponding spectrum for "uncoked" Ni is also shown, although it is featureless due to the lack of active Raman modes in the Ni metal itself.

Presented in Fig. 2a is an optical micrograph of a ≈100 μm wide area on the surface of the same Ni coupon along with a Raman

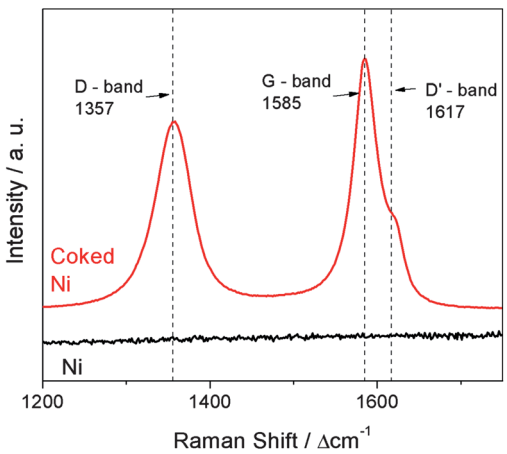

Fig. 1 Typical Raman spectrum collected in air from a spot on the surface of a Ni coupon before (black trace) and after exposure to C_3H_8-containing gas at 550 °C (red trace). The spectral band assignments highlighting characteristic carbon features are indicated by the arrows.

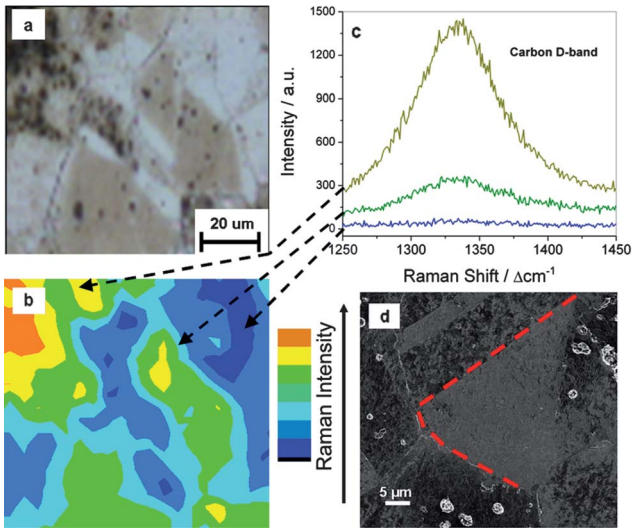

Fig. 2 (a) Optical micrograph of a Ni coupon after exposure to C_3H_8-containing gas at 550 °C along with (b) a map of carbon D-band Raman intensity (integrated from 1270–1445 cm^{-1}) collected from the same area. (c) Actual spectra from selected spots of the map. (d) SEM micrograph of the same Ni coupon. Note that some of the grain boundaries are indicated by dotted red lines.

intensity map for the carbon D-band of the same area (Fig. 2b). Example spectra from a few of the mapped spots are shown in Fig. 2c. From the optical micrograph, varying areas of discoloration with loose black particles in some places can be seen on the Ni surface, suggesting different levels of coking within the imaged area. The corresponding Raman map was plotted using a ratio of the integrated intensity for the D-band (area under 1250–1445 cm^{-1}) and the background signal. A direct correlation between higher carbon D-band intensities and higher levels of discoloration can be observed from the map and micrograph, indicating that the Raman mapping is a viable semi-quantitative indicator of how the carbon distribution varies across the Ni surface. This capability is important for understanding coking and the corresponding tolerance phenomena since knowing where the carbon deposits give clues about the relevant mechanisms.

These results indicate that initial coking was not homogeneous across the nickel surface. By examining different areas of the surface using scanning electron microscopy (SEM), we found clear grain boundaries that appear to separate regimes of carbon deposition, which was indicated by areas of dark discoloration (Fig. 2d). Since this nickel coupon is polycrystalline and grains with different orientations will exhibit different crystal planes when they are polished, it is most likely that the heterogeneity in coking levels originated from varying propensities for carbon deposition across different crystal planes. A similar relationship between crystal plane orientations and coking tendencies was reported previously.[38] Finally, the micrograph in Fig. 2d also shows that coking within some grains formed discontinuous, non-solid-colored patterns. Since the sample examined had been exposed to C_3H_8 for a relatively short time, the patterns observed might be related to the initial appearance and growth of carbon nuclei in favorable locations. Besides the contrasts shown in the optical image, SEM and Raman mapping, coking also produced morphological distortions on the polycrystalline nickel surface (Fig. ESI-2†).

On the other hand, of greater interest to those in the field of SOFC research is where and how carbon actually deposits during coking processes in multi-phase or composite anodes which contain Ni. To address this issue, electrodes with well-defined boundaries *vis-á-vis* YSZ substrates[31,32] were used in this work. A further demonstration of *ex situ* mapping of carbon deposited on a strip-patterned Ni sample is given in the ESI (Fig. ESI-3†). While the information gleaned from the *ex situ* experiments is certainly interesting, similar findings have been reported by others in previous studies.[22,23] Furthermore, one could have reached the same information by more conventional surface methods like electron spectroscopies. The true advantage of Raman spectroscopy and mapping lies in the possibility of *in situ* analysis of SOFC anodes; specifically, the technique can be used to probe and map anode surfaces under cell operating conditions.

For the current *in situ* Raman work, the Ni and Cu electrodes were directly analyzed *during* exposure to typical CH_4 or C_3H_8 fuel gases at high temperature in an environmental chamber. To demonstrate the Raman spectroscopy's ability to spatially map carbon deposition under *in situ* conditions, a strip-patterned Ni electrode was analyzed while exposed to CH_4 at 625 °C in the environmental chamber. After 12 hours of exposure, a map of the integrated intensity in the 1200–1700 cm^{-1} range was collected from the area marked in Fig. 3a. The integrated intensity from this range includes the D-band, G-band, and D′-band. By comparing the spectrum in Fig. 1 with its analogs in Fig. 3b, the high analysis temperature led to notable broadening of the Raman features, reduction in intensity, and increased background noise from more thermal vibrations. These spectral changes limited the amount of available Raman signal, so the entire range was used instead of a single Raman mode in order to maximize success in

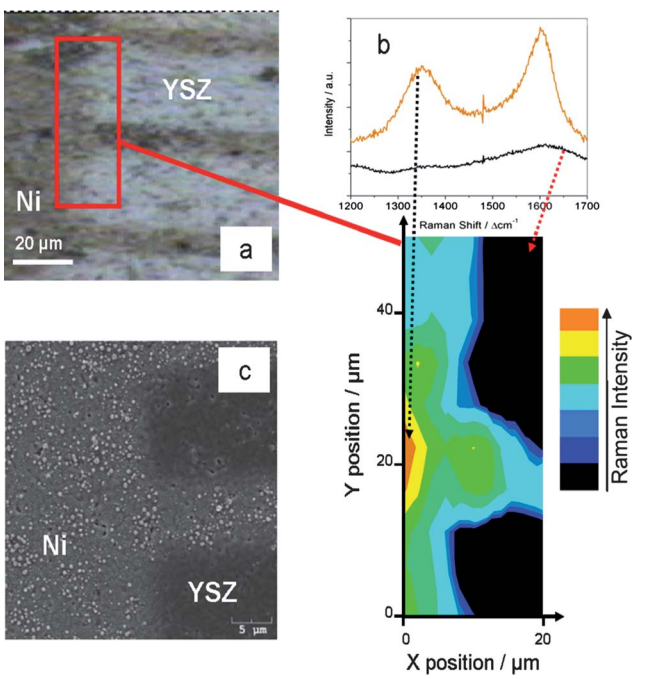

Fig. 3 (a) Optical micrograph of a strip-patterned electrode exposed to CH_4 gas at 625 °C. (b) Raman spectra and intensity map of the total carbon signal collected *in situ* from the area marked in (a) at the 12 hour mark during CH_4 exposure. (c) SEM image of the patterned electrode following CH_4 treatment.[37]

detecting the total amount of carbon. In addition, these factors also reduced the image resolution as compared to *ex situ* experiments. Fortunately, as can be seen in these spectra, the YSZ band near 1600 cm^{-1} was not so prominent at high temperature; the suppression of this band makes the deconvolution of the carbon signal into its constituent bands, and therefore identification of the forms of carbon present, an easier task.

Moreover, as Fig. 3b shows, the relevant signal was detected almost exclusively from the Ni surface, indicating that coking preferentially occurs there. This observation is supported by SEM imaging over the same area that was performed after cooling down and removing the sample from the chamber. As shown in Fig. 3c, nodule-shaped particles were only visible on the Ni surface. These particles were not present on the Ni surface before exposure to CH_4 and were thus likely related to carbon deposition. The particle deposition pattern appeared to be discontinuous, and the particles themselves were only 10–100 nm in size.

The same atmosphere and temperature treatment was also applied to YSZ pellets with Cu electrodes, and Raman spectra were collected *in situ* from the Cu surface. Cu was chosen for comparison due to its lack of strong catalytic activity towards carbon formation.[12] As expected, the acquired spectra confirmed that carbon formation does not occur on Cu as aggressively as it does on Ni under the same conditions (Fig. ESI-4†).

For subsequent demonstrations of the capability of Raman spectroscopy for *in situ* monitoring of carbon deposition at specific microscale electrode sites over time, Ni mesh electrodes embedded in YSZ were used *in lieu* of the strip-patterned electrodes. While the strip-patterned electrodes served as an ideal test bed for an initial fundamental demonstration of the ability to map deposited carbon on anode surfaces, the mesh electrodes would ultimately be more suitable for serving as *functional* anodes that could be simultaneously characterized by Raman spectroscopy methods and electrochemical testing; the mesh samples are easier to fabricate by conventional ceramic processing and would allow for more efficient current collection. Efforts towards coupling electrochemical SOFC tests with the Raman techniques outlined here, while not covered in this work, are ongoing.

For *in situ* experiments involving the monitoring of carbon deposition on Ni mesh electrodes, C_3H_8-containing gas was used instead of CH_4 to provide a more aggressive test of coking resistance. The gas was bubbled through water before entering the chamber *in lieu* of electrochemically producing the water at the electrode. Finally, the Ni mesh was modified with BaO using methods very similar to those described in Yang *et al.*[4] in order to promote water adsorption of the anode and directly evaluate its effect on coking tolerance.

Fig. 4a displays an optical micrograph of an unmodified Ni mesh electrode at 625 °C in reducing atmosphere (to prevent undesired Ni oxidation) directly before introduction of C_3H_8. After C_3H_8 began flowing into the chamber, spectra were collected periodically from a spot on the surface of a sample of the Ni mesh. This spot is marked by the green dot in Fig. 4b, which shows the mesh after 15 hours of wet C_3H_8 exposure at 625 °C. Some extent of the damage to the mesh caused by coking can be seen in the micrograph by itself. Nonetheless, Raman spectra collected from the Ni mesh and YSZ substrate (Fig. 4c) once again demonstrated that a carbon signal was only detectable on the Ni surface; the spectrum from the substrate showed only YSZ features.

A plot of the change in relative carbon signal intensity over the first few hours of exposure time is shown in Fig. 4d. The intensity of the carbon signal increased as carbon built up on the surface of the Ni from coking. The amount of detectable carbon signal eventually leveled off after a few hours, which was likely due to the thickness of the deposited carbon on the Ni exceeding the penetration depth of the Raman excitation. A Ni mesh sample modified by BaO was subjected to the same experimental conditions. The surface of the modified Ni sample during wet C_3H_8 exposure at 625 °C is shown in Fig. 4e. The micrograph was captured at the 15 hour mark near the Ni–YSZ interface. The spots that can be observed on the Ni surface were confirmed to be the result of the modification treatment, since they

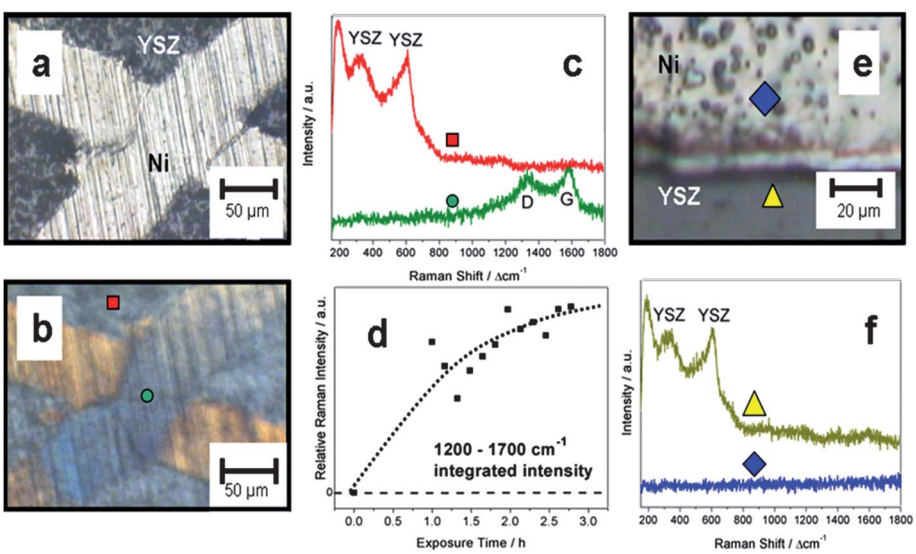

Fig. 4 (a) Optical micrograph of the Ni mesh embedded in YSZ. (b) The same embedded Ni mesh after exposure to C_3H_8-containing gas at 625 °C for 15 hours. (c) Raman spectra collected *in situ* from the spots marked in (b) at the 15 hour mark of C_3H_8-containing gas exposure. (d) Plot of change in carbon Raman signal intensity collected over time from the green circle spot on the Ni mesh marked in (b). (e) Optical micrograph near the interface of the BaO-modified Ni mesh and YSZ during the same C_3H_8 treatment. (f) Raman spectra collected *in situ* at the 15 hour mark from spots marked in (e).

were present on the modified Ni prior to any exposure to C_3H_8 and did not change afterward. Fig. 4f displays Raman spectra collected from the marked spots on the modified sample. The carbon signal was not detectable even on the Ni surface in this case. In contrast, spectra collected from both unmodified and modified Ni that were simultaneously exposed to dry C_3H_8 at high temperature (see Fig. ESI-5†) demonstrated nearly equal amounts of coking, indicating that the BaO surface modification conveyed significant coking resistance to the Ni only in the presence of water. This information supports the hypothesis that BaO particles help utilize water to stave off carbon deposition.

Raman spectroscopy has demonstrated great applicability in mapping and monitoring carbon on Ni-based SOFC anodes under *ex situ* as well as *in situ* conditions. Direct evidence of preferential coking on the Ni surface with little to no coking YSZ was provided, and the growth of carbon on the Ni surface was successfully monitored over time at high temperature. In addition, this technique provided additional evidence of the roles that water and BaO modification play in coking resistance on the Ni anode, which is useful information for further improving the anode design.

The electrodes with well-defined boundaries used in this work facilitated the mapping and monitoring experiments. These types of electrodes, particularly the mesh design, can be readily applied to Raman experiments involving the application of both chemical and electrochemical stimuli. Current efforts are focused on coupling electrochemical measurements with the Raman techniques described herein to gain additional insight into the mechanisms of coking and its prevention on the SOFC anode.

Acknowledgements

This work was supported by the HeteroFoaM Center, an Energy Frontier Research Center funded by the U.S. Department of Energy, Office of Science, Office of Basic Energy Sciences (BES) under Award Number DE-SC0001061. The authors would also like to thank Dr Erik Koep for preparation of strip-patterned Ni electrodes.

References

1 N. Q. Minh, *Solid State Ionics*, 2004, **174**, 271–277.
2 M. Liu, M. E. Lynch, K. Blinn, F. Alamgir and Y. Choi, *Mater. Today*, 2011, **14**, 534–546.
3 L. Yang, S. Wang, K. Blinn, M. Liu, Z. Liu, Z. Cheng and M. Liu, *Science*, 2009, **326**, 126–129.
4 L. Yang, Y. Choi, W. Qin, H. Chen, K. Blinn, M. Liu, P. Liu, J. Bai, T. A. Tyson and M. Liu, *Nat. Commun.*, 2011, **2**, 357.
5 A. Atkinson, S. Barnett, R. J. Gorte, J. T. S. Irvine, A. J. McEvoy, M. Mogensen, S. C. Singhal and J. Vohs, *Nat. Mater.*, 2004, **3**, 17–27.
6 Y. Lin, Z. Zhan, J. Liu and S. A. Barnett, *Solid State Ionics*, 2005, **176**, 1827–1835.
7 O. A. Marina, N. L. Canfield and J. W. Stevenson, *Solid State Ionics*, 2002, **149**, 21–28.
8 J. C. Ruiz-Morales, J. Canales-Vazquez, C. Savaniu, D. Marrero-Lopez, W. Zhou and J. T. S. Irvine, *Nature*, 2006, **439**, 568–571.
9 Y. H. Huang, R. I. Dass, Z. L. Xing and J. B. Goodenough, *Science*, 2006, **312**, 254–257.
10 W. A. G. McPhee, L. Bateman, M. Koslowske, M. Slaney, Z. Uzep, J. Bentley and T. Tao, *J. Fuel Cell Sci. Technol.*, 2011, **8**, 041007.
11 M. Cimenti and J. M. Hill, *Energies*, 2009, **2**, 377–410.
12 N. M. Galea, D. Knapp and T. Ziegler, *J. Catal.*, 2007, **247**, 20–33.
13 M. F. Liu, Y. M. Choi, L. Yang, K. Blinn, W. Qin, P. Liu and M. L. Liu, *Nano Energy*, 2012, **1**, 448–455.
14 A. Stierle and A. M. Molenbroek, *MRS Bull.*, 2007, **32**, 1001–1009.
15 A. C. Ferrari and J. Robertson, *Phys. Rev. B: Condens. Matter*, 2001, **64**, 075414.
16 M. S. Dresselhaus, A. Jorio, M. Hofmann, G. Dresselhaus and R. Saito, *Nano Lett.*, 2010, **10**, 751–758.
17 S. Zha, A. Moore, H. Abernathy and M. Liu, *J. Electrochem. Soc.*, 2004, **151**, A1128–A1133.
18 M. B. Pomfret, J. C. Owrutsky and R. A. Walker, *J. Phys. Chem. B*, 2006, **110**, 17305–17308.
19 M. B. Pomfret, J. Marda, G. S. Jackson, B. W. Eichhorn, A. M. Dean and R. A. Walker, *J. Phys. Chem. C*, 2008, **112**, 5232.
20 B. C. Eigenbrodt, M. B. Pomfret, D. A. Steinhurst, J. C. Owrutsky and R. A. Walker, *J. Phys. Chem. C*, 2011, **115**, 2895.
21 C. Su, R. Ran, W. Wang and Z. P. Shao, *J. Power Sources*, 2011, **196**, 1967–1974.
22 M. Yoshinaga, H. Kishimoto, M. E. Brito, K. Yamaji, T. Horita and H. Yokokawa, *J. Ceram. Soc. Jpn.*, 2011, **119**, 307–309.
23 H. Sumi, P. Puenggjinda, H. Muroyama, T. Matsui and K. Eguchi, *J. Power Sources*, 2011, **196**, 6048–6054.
24 X. Li, K. Blinn, Y. Fang, M. Liu, M. A. Mahmoud, S. Cheng, L. A. Bottomley, M. El-Sayed and M. Liu, *Phys. Chem. Chem. Phys.*, 2012, **14**, 5919–5923.
25 H. Z. Yang, Y. Q. Yang and S. Z. Zou, *J. Phys. Chem. B*, 2006, **110**, 17296–17301.
26 Y. M. Choi, H. Abernathy, H.-T. Chen, M. C. Lin and M. Liu, *ChemPhysChem*, 2006, **7**, 1957–1963.
27 K. S. Blinn, H. W. Abernathy and M. L. Liu, *Advances in Solid Oxide Fuel Cells V*, 2010, **30**, 65.
28 V. V. Pushkarev, V. I. Kovalchuk and J. L. d'Itri, *J. Phys. Chem. B*, 2004, **108**, 5341–5348.
29 R. C. Maher and L. F. Cohen, *J. Phys. Chem. A*, 2008, **112**, 1497–1501.
30 B. Tiwari, A. Dixit and G. P. Kothiyal, *Int. J. Hydrogen Energy*, 2011, **36**, 15002–15008.
31 H. Abernathy, E. Koep, C. Compson, Z. Cheng and M. Liu, *J. Phys. Chem. C*, 2008, **112**, 13299–13303.
32 Z. Cheng, H. Abernathy and M. Liu, *J. Phys. Chem. C*, 2007, **111**, 17997–18000.
33 Z. Cheng and M. Liu, *Solid State Ionics*, 2007, **178**, 925–935.
34 Z. Cheng, J.-H. Wang, Y. M. Choi, L. Yang, M. C. Lin and M. Liu, *Energy Environ. Sci.*, 2011, **4**, 4380–4409.
35 M. B. Pomfret, D. A. Steinhurst and J. C. Owrutsky, *Energy Fuels*, 2011, **25**, 2633–2642.
36 E. Koep, C. Compson, M. L. Liu and Z. P. Zhou, *Solid State Ionics*, 2005, **176**, 1–8.
37 H. W. Abernathy, PhD thesis, Georgia Institute of Technology, 2008.
38 J. Zhang, C. Kong and D. J. Young, *Mater. High Temp.*, 2009, **26**, 45–55.